

# A QUANTITATIVE ANALYSIS OF TOUGHENING MECHANISMS IN STEEL FIBRE REINFORCED ULTRA-HIGH-PERFORMANCE CONCRETE THROUGH MULTIMODAL NONDESTRUCTIVE EVALUATION

DMITRY LOSHKOV, YI PENG, ROMAN KRAVCHUK AND ERIC N. LANDIS

University of Maine  
Orono, Maine USA  
e-mail: landis@maine.edu

**Key words:** X-ray Computed Tomography, Acoustic Emission, Fiber Reinforced Concrete

**Abstract.** For the joint purposes of better informed meso-scale models and for more rational for “materials by design” concepts, we seek to isolate and measure the different mechanisms that lead to high strength and high ductility of steel fiber reinforced ultra-high-performance concrete (UHPC). The work described here jointly applies quantitative x-ray computed tomography (CT) and acoustic emission (AE) techniques to monitor and measure damage progression in split cylinder tests of UHPC. 50-mm diameter specimens of two different fiber types were CT scanned both before and after load testing. From the resulting images, fiber alignment was evaluated to quantify its effect on specimen performance. Results demonstrate the significance of fiber alignment, with best case being between 20 and 30% higher than the worst case. Cumulative AE energy was also affected commensurately. Post-test CT scans of the specimen were used to measure internal energy dissipation due to both matrix cracking and fiber pullout using calibration measurements for each. AE data, processed using an artificial neural network, was also used to classify energy dissipation. CT analysis showed that fiber pullout was the dominant energy dissipation mechanism, however, the sum of internal energy dissipation measured amounted to only 60% of the total energy dissipated by the specimens as measured by the net work of load. AE analysis showed a more balanced distribution of energy dissipation. AE data additionally showed how the dissipation mechanisms shift as damage accumulates.

## 1 INTRODUCTION

Toughening mechanisms in fiber reinforced cement-based composites have been well known and well documented for decades [1] [2]. Over the intervening years, much work has gone into optimizing different fiber and matrix types, fabrication techniques, and interfacial properties. In this work we seek to better quantify the micromechanical phenomena that dictates the performance of a fiber reinforced ultra-high performance concrete (UHPC). UHPC is typically defined by a high compressive strength ( $> 150$  MPa), and when combined with different types of reinforcing fibers leads to a

very high toughness material [3].

The overall goal of this work was to concurrently apply two complementary experimental techniques, x-ray computed tomography (CT) and acoustic emission (AE), to quantify the energy released during fracture of steel fiber reinforced UHPC specimens. By combining these two techniques, we are exploiting the best of what each offers. X-ray CT provides high-resolution 3D measurements of internal damage, but the information is available for only a limited number of fixed points during loading. Alternatively, AE monitoring does not provide the level of internal detail, but the information it

provides is real time, and the measurements can be tied to specific features of load-deformation curves.

The specific objective of this work was to characterize and quantify internal damage during split-cylinder fracture and to connect the damage mechanisms to overall load-deformation response. Two specific energy dissipation mechanisms were examined: matrix cracking and fiber pullout. Other mechanisms, such as fiber bending and fiber rupture, were previously found not to be significant. We hypothesize that we should be able to account for most of the total energy dissipated by the specimen during loading. However, in a split-cylinder configuration, there are additional mechanisms not directly associated with matrix cracking or fiber pullout. The influences of these additional mechanisms should manifest themselves in the differences between internal dissipation measurements and total external energy dissipation.

## 2 MATERIALS AND METHODS

### 2.1 UHPC Mix

The UHPC matrix used in this study was “Cor-Tuf” developed by the U.S. Army Engineer Research and Development Center (ERDC). The mix constituents are listed in Table 1, while details of the material and processing methods are presented in [4] and [5]. The cube strength of the unreinforced UHPC matrix was 170 MPa.

In this work, two different fibers were investigated: Dramix 30-mm-long 0.55-mm-diameter hooked-end steel fibers (ZP 305) and Bekaert 12-mm-long 0.20-mm-diameter straight brass-coated steel fibers (OL 13/.20). Both are of interest: the larger hooked-end fibers require a higher pullout force, but the smaller straight fibers can be better distributed through the matrix and are more likely to bridge cracks [6].

**Table 1:** Table of UHPC Constituents

Constituent	Mass (g)
Cement	621
Sand	600
Silica Flour	172
Silica Fume	241
Superplasticizer	11
Water	129

Four different UHPC specimen types were used for this work. All were nominal 50-mm-diameter cylinders. Three were cast as 50-mm diameter by 100-mm long, while one was cored from a larger UHPC block. The cored specimens were included to test an assumption that larger specimens (in this case the blocks from which the specimens were cored) are more likely to have a more uniform fiber alignment than specimens that are cast in a mold with dimensions only slightly larger than the fiber length. The assumption here is that fibers in cast specimens are more susceptible to the boundary effects of the specimen molds. In larger specimens, these effects are not as significant.

A summary of specimens tested, along with the naming nomenclature, is presented in Table 2. Among the four cylinders was one specimen that had no fibers. This specimen was used for baseline UHPC matrix fracture analysis. All specimens with fibers were prepared with a nominal fiber volume fraction of 3.5%.

**Table 2:** Summary of Different Specimen Types

Designation	Fiber Type	Fabrication
U	(no fibers)	Cast
Z	Dramix ZP305	Cast
B	Bekaert OL13/.20	Cast
Zc	Dramix ZP305	Cored

### 2.2 X-Ray CT Imaging

Each of these specimens was scanned with a Northstar Imaging x-ray CT scanner at an acceleration voltage of 168 kV and a current of 230  $\mu$ A. The geometry of the scanning setup produced images with nominally 36- $\mu$ m voxels. (True resolution is closer to perhaps 50-70  $\mu$ m,

depending on relative contrast of phases.) Tomographic reconstruction volumes were nominally 1600 by 1600 by 3000 voxels for a volume domain of 58 by 58 by 108 mm. Renderings of these specimens are shown in Fig. 1. The renderings qualitatively illustrate the distribution of fibers in the specimens.

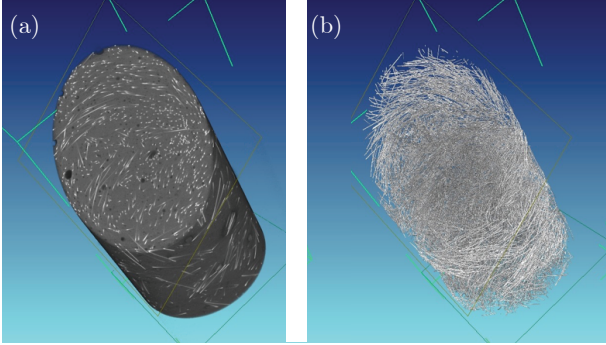


Figure 1: 3D renderings of undamaged cylinder. (a) shows a cutaway section; (b) shows same section but with UHPC matrix removed to reveal the fiber distribution and alignment.

Once scanning was complete, each of the four cylinders was cut in half with a diamond wet saw, resulting in two cylindrical specimens nominally 50 mm in diameter by 50 mm in length. The cut specimens provided a matched set for mechanical testing. Scanning was conducted on the uncut specimens to optimize x-ray time. The resulting 3D images of the undamaged specimens were electronically cut into two separate images to match the saw-cut specimens.

### 2.3 Optimum & Pessimism Orientations

Prior to mechanical testing, image data from each 50-mm by 50-mm specimen were analyzed to evaluate what we are defining here as the optimum and pessimism orientations for resistance to split-cylinder fracture. Qualitatively, the concept is easy to visualize. The plane of failure in a split cylinder is defined by the intersection of the specimen's cylindrical axis and its load axis. In the optimum orientation, fibers tend to have a larger component in a direction normal to this plane, while in the pessimism orientation, fibers tend to have larger components

that are parallel to the failure plane. Fiber orientations were evaluated by using a 3D fiber orientation algorithm developed by Trainor *et al.* [7], which uses Hessian eigenvalue analysis at each fiber point to find the fiber orientation angle with respect to the axis of interest. Optimum and pessimism specimen orientations were evaluated by electronically rotating the specimen over a range of orientations,  $\Theta$ , relative to the load axis. At each  $\Theta$ , all relevant fibers were projected (direction cosine) onto an axis perpendicular to the plane of the load axis. These direction cosines were then summed for all relevant fibers. When this sum was the maximum, we refer to it as the optimum orientation. When the sum was the minimum, we refer to it as the pessimism orientation. Additional details can be found elsewhere. [8]

An illustration of the outcome of the analysis is presented in Fig. 2. Note that these images show only a small subset of fibers and are for illustrative purposes only. The full array of fibers is too dense to check by visual inspection.

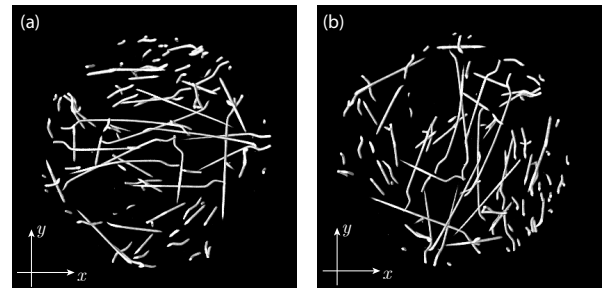


Figure 2: Images illustrating (a) optimum and (b) pessimism orientation of fibers for a small segment of the specimen. The load axis is oriented top to bottom in images. Only a small region is shown for better clarity.

### 2.4 Split Cylinder Tests

An Instron 5900R-4485 with the maximum capacity of 200 kN was used to perform split cylinder tests. Tests were performed under displacement control with a crosshead displacement rate set to 0.15 mm/minute. A pair of LVDTs was used to measure platen-to-platen displacement. Loading continued until the platen-to-platen displacement was approximately 3 mm. Fig. 3 shows the test setup.

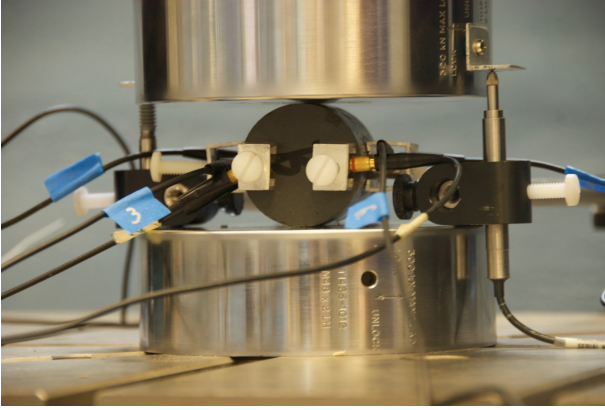


Figure 3: Photograph of split cylinder testing configuration. LVDTs measure platen-to-platen displacement, while six sensors are mounted on the specimen to capture AE activity.

Acoustic emission activity was monitored with a Digital Wave six-channel system. Full waveforms were recorded at 1-MHz sampling rate. Waveform length was 1024 points, or 1.024 milliseconds. Signals were detected with broad-band transducers attached to the specimen with screw-based mounting fixtures. The sensors were coupled to the specimens with vacuum grease. Care was made to make consistent sensor mounting so that measurements from different tests would be comparable. Prior to acquisition, signals were amplified 20 dB and subjected to a 20-kHz to 1.5-MHz band-pass filter.

### 3 Experimental Results

#### 3.1 Load-Deformation Results

Eight specimens were tested, two each of specimens designated as Z, Zc, B, and U. For the fiber-reinforced specimens (all but U), one specimen was tested in the optimum orientation, and one specimen was tested in the pessimism orientation. Fig. 4 shows the influence of fiber orientation on load-deformation response. In all cases, the optimum orientation produced both a higher peak load as well as a higher work of load (defined here as the area under the plot from zero to maximum deformation, less the elastic recovery.) A summary of these results is presented in Table 3.

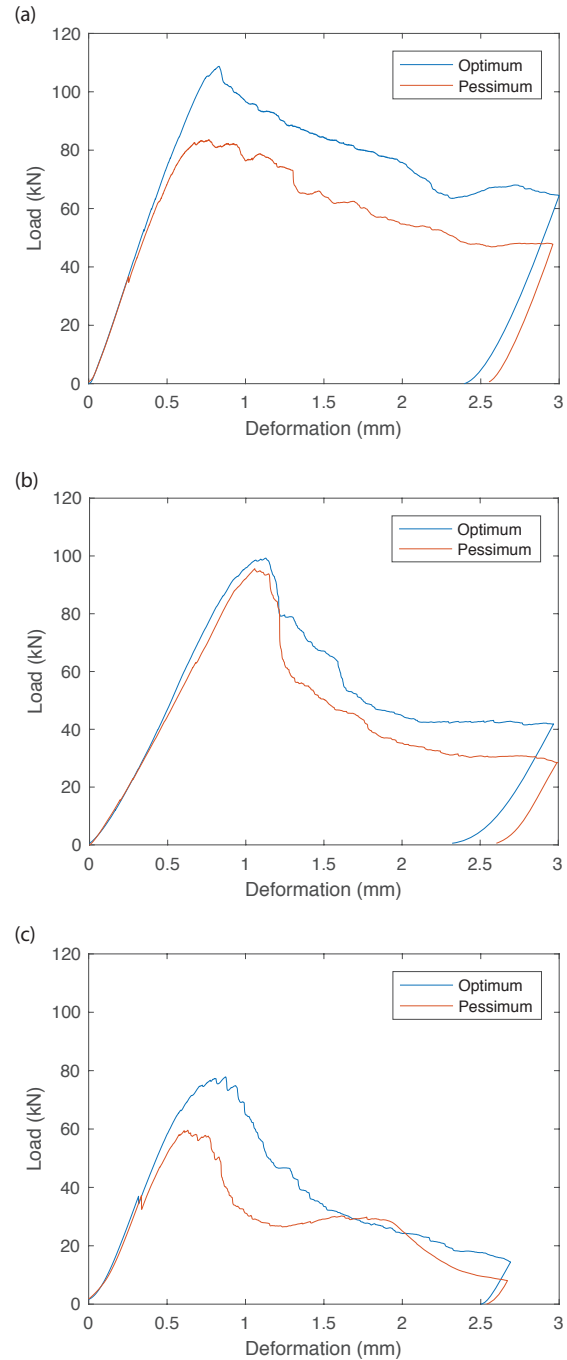


Figure 4: Load-deformation plots showing three specimen optimum/pessimism pairs. (a) “B” series, (b) “Z” series, and (c) “Zc” series.

Table 3: Peak load,  $P_{max}$ , and net work of load,  $W_{ext}$  for different specimens in optimum and pessimum orientations.

Designation	$P_{max}$ (N)		$W_{ext}$ (J)	
	Opt.	Pess.	Opt.	Pess.
B	110	84	183	148
Z	100	96	147	124
Zc	78	60	99	76

The B series specimens showed the highest overall net work of load, although the Z specimens both showed higher peak loads than the pessimum B specimen. We can likely attribute the higher energy absorption performance of the B specimens to the more uniform distribution of fibers. While hooked fibers require greater work for pullout of the UHPC matrix, the much larger number of the smaller means there are more fibers to bridge the cracks. The net result is higher overall toughness.

### 3.2 AE Results

AE activity was high with between 28,000 and nearly 65,000 individual events recorded per test. A number of parameters were extracted from the recorded waveforms, but because of the relevance to fracture energy, we were particularly interested in the energy released by each AE event. For this work, AE energy,  $E_{AE}$ , was evaluated by a time integration of the square of the recorded waveform, summed over all channels. Formally, the units of  $E_{AE}$  are volts-squared-times-time. However, since we are performing only relative comparisons, we simply denoted “relative units” for AE energy.

Sample results for the “B” and “Z” series are presented in Figs. 5(a) and (b). These two plots illustrate several important phenomena. First, they show *when* a majority of the AE energy is released. In all tests, the rate of energy release (slope of plot) is highest *before* the peak load is reached. Indeed, in each of these cases, the rate of AE energy release has already dropped by the time peak load is reached. Second, the plots show the differences in total energy release between the optimum and pessimum orientations. The total AE energy released is shown as the

right-most values on the plots. As seen in the figures, the greater the difference in specimen net work of load, the greater the difference in total AE energy measured. This relationship is not surprising, and will be useful for additional analysis described below.

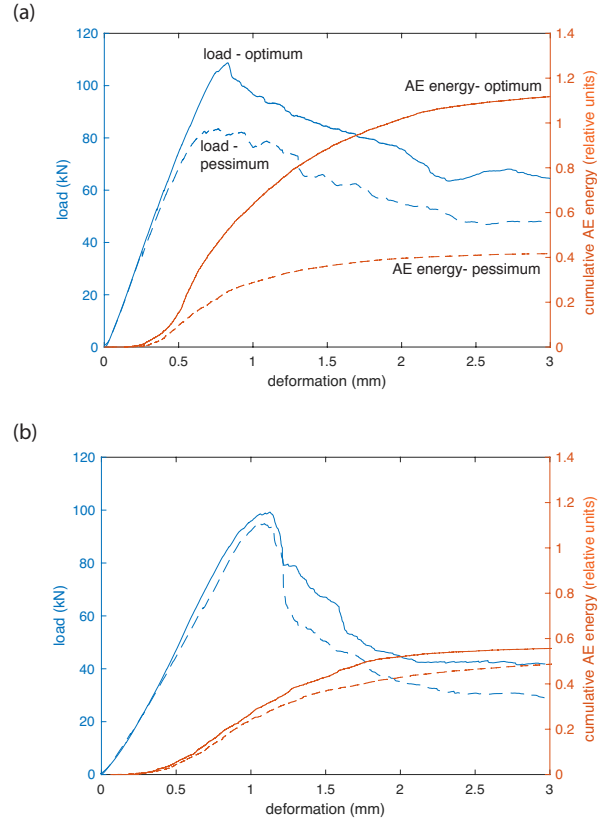


Figure 5: Load-deformation response and corresponding AE energy release for “B” series (a) and “Z” series (b) specimens.

## 4 Internal Damage Analysis

In order to quantify energy dissipation mechanisms, the eight damaged cylinder specimens were re-scanned with the same CT system. Care was taken to align the specimens in the same orientation as the original scans, and the scan parameters were set to record images with the same spatial resolution. It should be noted that, for the first set of scans (undamaged), the specimens were nominally 50-mm-diameter by 100-mm-long cylinders. For the second set of scans, (after saw cutting and testing), the specimens were nominally 50-mm-diameter by 50-mm-long cylinders. Eight scans were made, all at

a 36- $\mu\text{m}$  voxel size. In order to capture the entire specimen, the scan volumes were typically about 1600 by 1600 by 1600 voxels, for a total volume domain of about 58 by 58 by 58 mm.

Three-dimensional renderings of several specimens are shown in Fig. 6. The images illustrate both the internal crack networks that develop and the bridging of fibers across those crack networks. Fig. 6(a) further illustrates the damage pattern typically observed in these tests. Specifically, a large crack network forms along the axis of split cylinder loading as would be expected from the known stress distribution. However, because the fibers bridge the cracks, keeping them from expanding further, a triangular “plug” forms at one of the load points on the specimen. This plug features considerable compaction or plastic deformation such that the specimen flattens out.

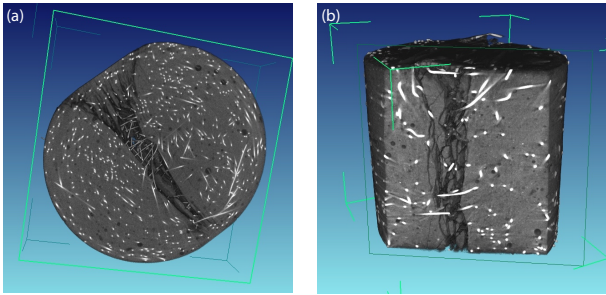


Figure 6: 3D renderings of (a) a B specimen (smaller fibers) and (b) a Z specimen (larger fibers). Images reveal the internal crack networks and the fibers that bridge those cracks. Note the flattened “plug” segment that appears on the upper left side of the B specimen (a). This flat side is typical of all the fiber-reinforced specimens.

#### 4.1 Energy Dissipation of Matrix Cracking

By using techniques developed by Trainor *et al.* [7] combined with newly developed techniques, the 3D image data collected before and after testing were analyzed to assess the influence of individual energy dissipation mechanisms. Specifically, energy dissipation was divided between the energy dissipated by matrix cracking and the energy dissipated by fiber pull-out.

In order to evaluate the energy dissipated by matrix cracking, a measurement of the specific

fracture energy of the UHPC matrix was made by testing an unreinforced specimen. Net work of load was measured using load-deformation data, and the resulting crack area was measured through a surface area measurement taken from post test CT scans. The specific fracture energy,  $G_f$ , is taken as simply the net work of load,  $U$ , divided by the crack area,  $A$

$$G_f = \frac{U}{A} \quad (1)$$

We note here that this fracture energy is based on a crack surface area that includes all parts of a tortuous crack network. That is, it includes branches and non-planar surfaces, not just an assumed planar crack area [9]. For the two unreinforced specimens evaluated here,  $G_f$  values of 84 J/m<sup>2</sup> and 96 J/m<sup>2</sup> were measured.

For reinforced specimens, the total energy dissipated by matrix cracking was determined by analyzing the total crack area created during the test and then multiplying that area by the specific fracture energy of the matrix material determined in the tests of unreinforced specimens described above. A technique similar to that used on the unreinforced specimens was applied to the reinforced specimens. That is, a simple 3D edge detection algorithm was applied to measure total surface area of specimens before and after testing. The difference in surface area measurements was then attributed to crack growth. Measured crack area ranged from  $3.2 \times 10^3 \text{ mm}^2$  to  $1.4 \times 10^3 \text{ mm}^2$ . Note that these crack areas are more than an order of magnitude greater than those found in the unreinforced specimens, illustrating the effect fibers have on inducing additional matrix cracking. Final estimates of energy dissipated by matrix cracking were made by multiplying the measured crack areas by the previously determined average specific fracture energy of 90 J/m<sup>2</sup>. That is

$$W_f = G_f \cdot A \quad (2)$$

where  $A$  is the measured crack surface area and  $W_f$  is the total energy dissipated by matrix cracking.

## 4.2 Energy Dissipation of Fiber Pullout

Our estimation of the energy dissipated by fiber pullout required a multi-step analysis. First, the length of fiber pulled out of the concrete matrix was measured, then the work required to pull that length of fiber out of the matrix was determined from individual fiber pullout calibration data. In order to measure the length of fiber pullout, a technique was developed based on the kinematic assumption that a fiber that is pulled out of the cement matrix must cross a crack. Furthermore, the total length of pullout must be the same as the sum of all cracks that the fiber crosses. Hence, the technique focuses on locations where fibers cross cracks.

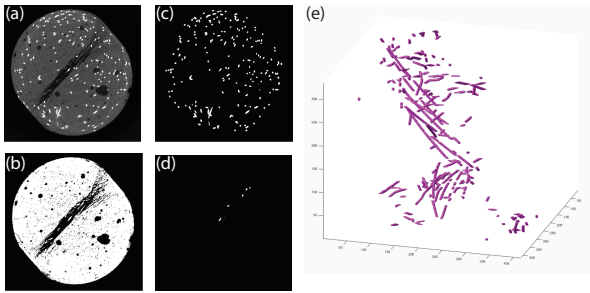


Figure 7: Fiber pullout length measurement: (a) original slice, (b) segmented to solid/void, (c) segmented to fibers only, (d) “masked” image in which fibers appear in cracks, and (e) 3D rendering of fibers exposed inside a crack.

The analysis can be illustrated by a series of images, presented in Fig. 7. Note that the images shown in the figure are 2D, but the analysis is done in 3D. First, the grayscale image is segmented into voids and solids. Next, the grayscale image is segmented to isolate fibers. These two operations can be conducted independently due to the significant differences in x-ray absorption between the steel fibers and the cement matrix. The two segmented images are combined such that the solids (Fig. 7[b]) provides a mask that can be applied to the fiber image (7[c]). The result is an image of fibers that cross cracks, as shown in 7(d). and illustrated in the 3D rendering of Fig. 7(e). Once the crack-crossing fiber segments are isolated,

their lengths can be measured.

Once the fiber bridge segments have been measured, the next step is to take those isolated fiber segments and use them to estimate the work of fiber pullout. A model fiber pullout curve was developed for each fiber type, based on fiber pullout experiments [10]. A key element of this work is that the effects of fiber confinement stresses on pullout response was investigated. A fixture was developed that allowed one to apply varying levels of confinement pressure on the concrete matrix surrounding the fiber. A total of 93 specimens were tested at one of the three different levels of confinement. Force-pullout curves were recorded for each test. Examples of such curves are shown in Fig. 8. The characteristic curve consisted of a rapid rise to a sharp peak, followed by a gradual post-peak descent to zero. These curves illustrate, in particular, the differences in the post-peak pullout response as a function of confinement stress.

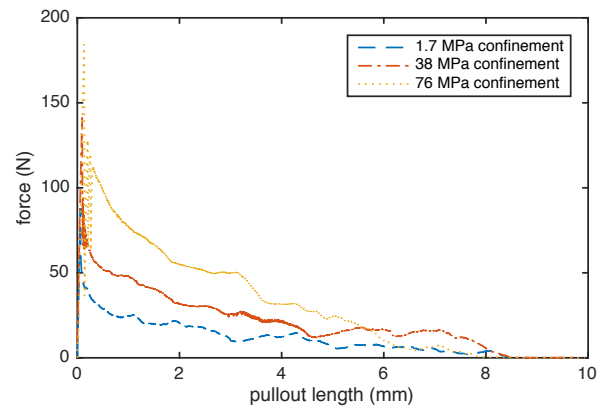


Figure 8: Typical force-pullout curves for three different confinement levels.

Based on these many measurements, an idealized curve was developed based on the work of Lin *et al.* [11], who developed a model in which the the force-pullout response,  $P(v)$ , is a function of the fiber-matrix bond-fracture energy,  $G_d$ , the fiber-matrix interface-friction stress,  $\tau_0$ , and several geometric properties. In this work the bond energy and interface friction were determined from the pullout experiments, and the geometric properties were mea-

sured from the CT images. An example pullout curve is shown in Fig. 9 along with sample experimental data.

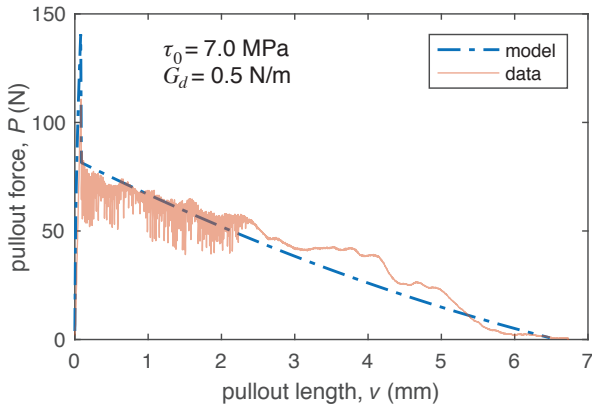


Figure 9: Plot of fiber force-pullout response model used for fiber pullout energy contribution.

Given this model for the pullout response, the work to pullout that fiber is estimated by integrating the model pullout curve over the distance the fiber has pulled out, that is,

$$w_p = \int_0^l P(v) dv \quad (3)$$

where  $w_p$  is the work required to pull out the fiber,  $P(v)$  is the model pullout function, and  $l$  is the length of pullout, which equals the length of the fiber bridge. This is repeated for all fibers so that the total energy dissipated by fiber pullout,  $W_p$ , is simply

$$W_p = \sum_{i=1}^N (w_p)_i \quad (4)$$

where  $i$  indicates a particular fiber, and  $N$  is the total number of fibers pulled out (68 separate fiber segments for the specimen illustrated in Fig. 7).

It should be noted that the magnitude of the force-pullout curves was found to be dependent on the lateral stress in the concrete matrix [10]. As the split cylinder test puts the critical crack bridging fibers into a compression field, the model pullout curve used in eq. (3) accounted for this effect.

### 4.3 Total Energy Dissipation

An initial assumption in this work is that the primary mechanisms for energy dissipation in UHPC are matrix cracking and fiber pullout. If this is true, we can simply add the quantities determined through eqs. (2) and (4)

$$W_{int} = W_f + W_p \quad (5)$$

where  $W_{int}$  is the total internal energy dissipation. We define  $W_{int}$  as distinct from the net work of load,  $W_{ext}$ , presented in Table 3. Since the two need to be equal, a comparison of  $W_{int}$  with  $W_{ext}$  provides us with a convenient check of our measurements.

The results of this energy accounting are presented in Table 4 for all specimens. The table presents the matrix cracking component,  $W_f$ ,

Table 4: CT-based breakdown of measured energy dissipation in different specimens

Specimen	Energy (J)			
	$W_f$	$W_p$	$W_{int}$	$W_{ext}$
B-opt.	22	88	110	183
B-pess.	19	72	91	148
Z-opt.	29	80	109	147
Z-pess.	21	27	48	124
Zc-opt.	13	41	54	99
Zc-pess.	12	32	44	76

the fiber pullout component,  $W_p$ , the total internal dissipation,  $W_{int}$ ; and the external work of load,  $W_{ext}$ .

The first general observation from the results of Table 4 is that (with all but one exception) fiber pullout dissipates between three and four times more energy than matrix cracking. There does not seem to be a distinction in this distribution between optimum and pessimum orientations, but we would not necessarily expect there to be. We would only expect the total amounts to vary commensurately, which they do.

The second general observation is that the total internal energy dissipation is typically less than two thirds of the external net work of load work, indicating that a significant amount of internal energy dissipation is not accounted for in this analysis.

It is worth noting that in the case of hooked fibers, there is energy dissipation associated with plastic deformation. Specifically, the fibers bend as they are pulled out. In this analysis, that energy is included with the energy of pull-out. Since the pullout forces for these fibers is well below the force required for yield, we assume little to no plastic deformation associated with axial yield. Additionally, Trainor *et al.* [7] showed that plastic deformation due to fiber bending is negligible.

#### 4.4 AE Analysis of Energy Dissipation

Each AE event was classified using an artificial neural network trained using a combination of unsupervised and supervised learning. [12] Using the trained network, events were classified matrix cracking, fiber pullout, or unclassified. Once an event was classified, its energy could be calculated as described in section 3.2 above. The total energy for each event type is shown in Table 5. Here we see that fiber pullout typically (although not always) releases more AE energy. This is somewhat consistent with the results found using CT analysis.

Table 5: AE-based breakdown of measured energy dissipation in different specimens. AE events are classified as matrix cracking (*Type 1*), fiber pullout (*Type 2*), and unclassified (*Type 0*)

Specimen	AE Energy ( $\times 10^4$ relative units)			
	<i>Type 1</i>	<i>Type 2</i>	<i>Type 0</i>	Total
B-opt	8.7	14.6	6.5	29.8
B-pess	4.8	3.4	3.0	11.1
Z-opt	5.1	7.7	2.6	15.4
Z-pess	6.9	8.2	3.1	18.2
Zc-opt	3.6	4.1	1.6	9.3
Zc-opt	4.2	3.7	1.8	9.7

The AE energy analysis becomes much more interesting when we examine the release of energy during the course of the test. Fig. 10 shows both load and cumulative AE energy release as a function of specimen deformation for one optimum/pessimum specimen pair. In both cases, very little AE energy accumulates until the load is between 50 and 75% of peak. Looking at the

source of the AE energy release, we further see that in both cases, the largest initial energy release is due to matrix cracking. However, for the optimum specimen, fiber pullout surpasses matrix cracking sometime shortly after peak load during the descending branch of the load curve. This result intuitively seems reasonable, as the energy dissipation of fiber pullout cannot be fully mobilized until there has been significant specimen deformation [10]. Thus, initial damage comes in the form of matrix cracking, but as cracks become sufficiently enlarged, the energy dissipation capacity of fiber pullout has a much larger effect.

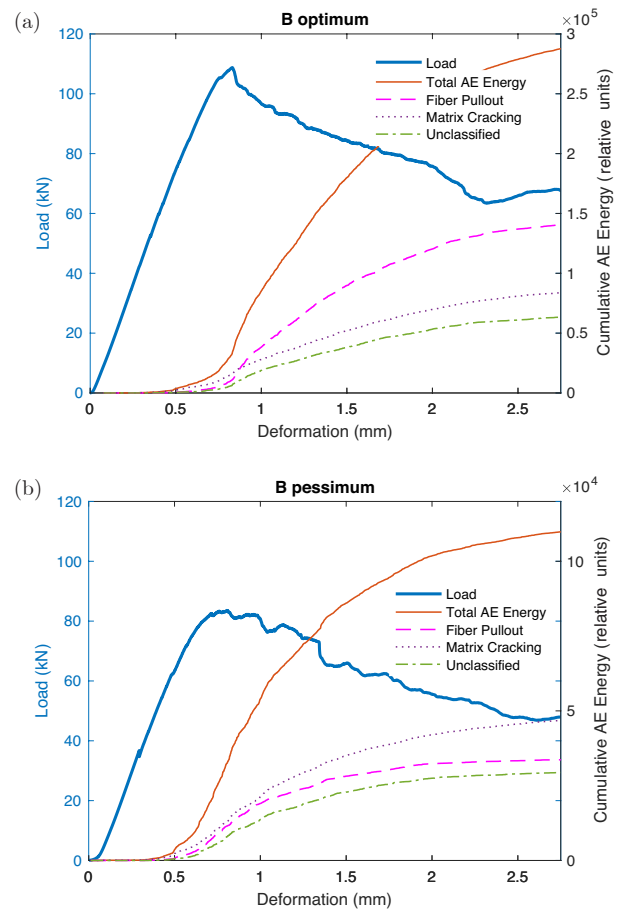


Figure 10: Load and cumulative AE energy release as a function of specimen deformation for specimen with smaller brass-coated steel fibers. Optimum orientation (a), pessimum orientation (b).

It should be emphasized, however, and this is perhaps among the more important findings of these experiments, is that energy dissipa-

tion of fiber pullout does not always surpass that of matrix cracking. In the example shown in Fig. 10(b), fiber pullout energy dissipation never catches up with that of matrix cracking. The specimen of this example was oriented at the pessimum position, meaning that the fibers have the lowest contribution to bridging principal tensile stresses. It would seem from this result that the spatial orientation distribution of fiber reinforcement in the specimen influences the distribution of internal energy dissipation.

## 5 DISCUSSION

The CT results show that, on average, we are able to capture about 60% of the internal energy dissipation in UHPC specimens subject to split cylinder loading. This is quite low compared to the nearly 90% that is captured using a similar approach for specimens subjected to three-point bending [7]. That said, our hypothesis all along has been that there are other mechanisms that manifest themselves in the split cylinder configuration. With regard to the AE results, a quick review of the net work of load presented in Table 3 shows that in all cases, the specimen loaded in the optimum position dissipated more total energy than the companion specimen loaded in the pessimum orientation. A review of the total AE energy recovered in each test (Table 5) does not show this consistency. In fact in two of the three cases, the pessimum orientation showed greater AE energy than the optimum. We suspect that the AE technique may show a slight bias toward the detection of matrix cracking compared to fiber pullout. That is, fiber pullout energy is slightly underrepresented. This would be the outcome if one assumes that much of the fiber pullout energy dissipation happens below the detection threshold of the AE measurement system.

With respect to these additional energy dissipation mechanisms, we submit two we can easily identify that are not accounted for in our analysis. Both can be qualitatively understood by an examination of the cross-sectional rendering of Fig. 6(a). In this specimen, we see the main crack network along the axis of the

load. In addition, we see two things at the top of the (upper left-hand side of image) specimen that are relevant. The first is the flattened region where the specimen was in contact with the platen. This flattening cannot occur unless there is another mechanism introduced (*e.g.*, plastic deformation). In a traditional quasi-brittle material, plastic deformation is typically not considered significant, but the observation here is unquestionable. It may not be plastic deformation in the traditional sense in that there is not necessarily a “flow” of continuous material. More than likely it reflects a localized pulverizing and re-compaction of the material. This pulverization phenomenon would not necessarily be visible through traditional x-ray CT image analysis, although we are considering ways in which such phenomenon may be reflected in the images. Regardless, if the analysis reported here is of similar accuracy as the beam tests of Trainor *et al.* [7], then the results here suggest that the combination of matrix compaction and crack friction add up to about 30% of total energy dissipation, which is comparable to the energy dissipated by fiber pullout.

The second mechanism that can be qualitatively observed in Fig. 6(a) is the wedge that appears below the previously mentioned flattened section. If a wedge is moving through the damaged split cylinder, there must be friction associated with that movement. Indeed, it is likely these friction forces could be high, given the degree of confinement that the bridging fibers produce in the specimen. Unfortunately, there is no way to directly measure friction forces with the CT images, although Mondoringin and Ohtsu [13] were able to monitor sliding energy to a limited extent by using quantitative acoustic emission.

Finally, we acknowledge that the measurement techniques employed in this work have limitations. With respect to matrix cracking, CT image resolution restricts our measurements to crack apertures greater than about 40  $\mu\text{m}$ . Undoubtedly, microcracks that are not visible in the CT images exist in the specimens. Current work-in-progress is aimed at solving this prob-

lem. With respect to AE analysis, there is reason to believe we are not able to capture all of the fiber pullout energy due to the lower amplitude of much of that activity. It is perhaps reasonable to propose that the actual distribution of energy dissipation is in between the bounds set by the two techniques. Through a new set of experiments we hope to narrow the degree of uncertainty.

## REFERENCES

- [1] A. Bentur and S. Mindess. *Fiber Reinforced Cementitious Composites*. Elsevier Science, London., 1990.
- [2] P.N. Balaguru and S.P. Shah. *Fiber-reinforced cement composites*. McGraw-Hill Companies, 1992.
- [3] FHWA. Ultra-high performance concrete. Tech Note FHWA-HRT-11-038, U.S. Federal Highway Administration, MacLean, VA, 2011.
- [4] Erin M Williams, Steven S Graham, Paul A Reed, and Todd S Rushing. Laboratory characterization of cor-tuf concrete with and without steel fibers. Technical Report ERDC/GSL TR-09-22, U.S. Army Engineer Research and Development Center, July 2009.
- [5] M Jason Roth, Todd S. Rushing, Omar G Flores, Devin K Sham, and Jamie W Stevens. Laboratory investigation of the characterization of cor-tuf flexural and splitting tensile properties. Technical Report ERDC/GSL TR-10-46, U.S. Army Engineer Research and Development Center, October 2010.
- [6] K Wille and A Naaman. Pullout behavior of high-strength steel fibers embedded in ultra-high-performance concrete. *ACI Materials Journal*, 109(4):479–487, 2012.
- [7] Kevin J. Trainor, Bradley W. Foust, and Eric N. Landis. Measurement of energy dissipation mechanisms in fracture of fiber-reinforced ultrahigh-strength cement-based composites. *Journal of Engineering Mechanics*, 139(7):771–779, 2013.
- [8] Eric N. Landis, Roman Kravchuk, and Dmitry Loshkov. Experimental investigations of internal energy dissipation during fracture of fiber-reinforced ultra-high-performance concrete. *Frontiers of Structural and Civil Engineering*, 13(1), 2019.
- [9] S C de Wolski, J E Bolander, and E N Landis. An In-Situ X-Ray Microtomography Study of Split Cylinder Fracture in Cement-Based Materials. *Experimental Mechanics*, 54(7):1227–1235, May 2014.
- [10] Arden C. McSwain, Keith A. Berube, Gianluca Cusatis, and Eric N. Landis. Confinement effects on fiber pullout forces for ultra-high-performance concrete. *Cement and Concrete Composites*, 91:53–58, 2018.
- [11] Z Lin, T Kanda, and V C Li. On interface property characterization and performance of fiber-reinforced cementitious composites. *Concrete Science and Engineering*, 1:173–184, September 1999.
- [12] Roman Kravchuk and Eric N. Landis. Acoustic emission-based classification of energy dissipation mechanisms during fracture of fiber-reinforced ultra-high-performance concrete. *Construction and Building Materials*, 176:531–538, 2018.
- [13] Mielke R. I. A. J. Mondoringin and Masayasu Ohtsu. Kinematics on split-tensile test of fiber-reinforced concrete by AE. *Journal of Advanced Concrete Technology*, 11(8):196–205, 2013.